Mineral replacement rate of olivine by chrysotile and brucite under high alkaline conditions

Romain Lafay, German Montes-Hernandez, Emilie Janots, Rodica Chiriac, Nathaniel Findling, François Toche

Mineral replacement rate of olivine by chrysotile and brucite under high alkaline conditions

Romain Lafay [1*], German Montes-Hernandez [1*], Emilie Janots[1], Rodica Chiriac[2], Nathaniel Findling[1], Francois Toche[2]

[1] Institut des Sciences de la Terre (ISTerre), UJF-CNRS, F-38041, Grenoble I, Cedex 9, France

[2] Université Lyon 1, Laboratoire des Multimatériaux et Interfaces UMR CNRS 5615, 43 bd du 11 novembre 1918, 69622 Villeurbanne Cedex, France

* Corresponding authors: Romain Lafay (romain.lafay@ujf-grenoble.fr) and G. Montes-Hernandez (german.montes-hernandez@obs.ujf-grenoble.fr)

Abstract

Olivine mineral replacement by serpentine is one major alteration reaction of oceanic hydrothermalism. In the present experimental study, olivine grains were replaced by chrysotile and brucite under high alkaline conditions. In our study, olivine replacement implied a spatial and temporal coupling of dissolution and precipitation reactions at the interface between olivine and chrysotile-brucite minerals. Coupled dissolution-precipitation led to the alteration of starting olivine grains (so-called primary or parent mineral) to a porous mineral assemblage of chrysotile and brucite with preservation of the initial olivine morphology. This mineral replacement reaction of olivine (serpentinization) has been characterized using XRD, FESEM and FTIR measurements. Moreover, a simple and novel method is here proposed to quantify the mineral replacement rate (or serpentinization rate) of olivine by using thermogravimetric (TG) and differential TG (DTG) analyses. Serpentinization extent depends on the grain size: it is complete after 30 days of reaction for the smallest olivine grains (<30μm), after 90 days of reaction for the intermediate olivine grains (30 μm-56 μm) and reaches 55% of olivine replacement after 90 days for the largest fraction (56-150 μm). Based on the fitting of the serpentinization extent (ξ_t) versus time (t) by using a kinetic pseudo-second-order model, the serpentinization rates vary from 3.6×10^{-6} s^{-1} to 1.4×10^{-7} s^{-1} depending on the olivine grain size. An additional correlation between FTIR spectra analysis and TG measurements is proposed. The mineral replacement reactions frequently observed in natural alteration processes could be a powerful synthesis route to design new porous and/or nanostructured materials.

Keywords: A1. Serpentinization; A1. Mineral replacement rate; B1. Alkaline medium; B2. Chrysotile nanotubes; A1. TG analyses

1 Introduction

Serpentine minerals (chrysotile, lizardite and antigorite) are widespread in Earth oceanic lithosphere and are frequently found in chondrites and other extraterrestrial objects. Serpentine mineralization is of great interest in several fields of research. Serpentinized rocks present a great enrichment in trace elements compared to primary mantle rocks [1–6]. Serpentine appears as a vector for trace elements between crustal and mantle reservoirs [2,5,7,8]. Experimental studies have tested the influence of major (e.g. Fe, Ni) and/or trace elements (e.g. Li) on the growth of serpentine [9–14]. This kind of synthesis experiments presents a great interest in medical research due to the asbestos toxicity that can be induced by inhalation of magnesium silicates fibers including chrysotile [15–18]. Serpentine minerals are also crucial for sequestration of CO_2 due to its availability and sequestration capacity [19–21]. Indeed a lot of studies are looking for technologies that could possibly contribute to reduce carbon dioxide emissions. Geological sequestration and ex-situ mineralization of CO_2 using serpentine could be one of the most efficient methods considering the enormous quantity of serpentine on Earth [22].

In meteorites, serpentine minerals are directly linked to aqueous alteration processes and reaction conditions (e.g. [23] and references therein). In the oceanic lithosphere, serpentines result from interaction between mantle rocks (peridotite composed by olivine and pyroxenes) and hydrothermal fluids, generally with high fracturation dynamic [24,25]. Olivine alters along grain boundaries and fractures to produce a mesh texture that preserves the original olivine morphology at the grain scale [26,27]. This olivine replacement by serpentine is best explained by coupled dissolution-precipitation processes [28–30]. This reequilibration process leads to the replacement of one pristine mineral by a secondary mineral (or assemblage) with a lower solubility in the fluid. Replacement occurs at the fluid/solid interface maintaining the original external grain shape (pseudomorphism). During alteration, a secondary porosity is

commonly produced due to volume difference between pristine and secondary minerals, material loss during dissolution and grain fracturation [24,25]. Secondary porosity enables the fluid to move interstitially towards the reaction front until the complete mineral replacement reaction. In oceanic lithosphere, peridotite replacement, and consequent element redistribution associated with this alteration, is primarily controlled by the physic-chemical conditions of the hydrothermal fluid (Temperature, Pressure, fluid speciation, pH). Fluids escaping from deep sea hydrothermal vents show a large variety of composition and pH, reflecting a large range of possible physic-chemical conditions. Amongst them, alkaline fluids with high pH were collected in some hydrothermal fields (e.g., [31,32]).

Numerous experimental studies were conduct to reproduce serpentinization in hydrothermal context [33–40] and explain serpentine growth [41]. Kinetic appears faster under alkaline conditions [40,42] but few recent studies have addressed the role of pH on serpentinization kinetic, particularly in alkaline conditions.

In the present experimental study, we have investigated the process and kinetics of olivine serpentinization in alkaline hydrothermal conditions (pH = 13.5, measured at 25°C). Experimental products were characterized using XRD, FESEM and FTIR. The serpentinization rate was determined using a simple and novel method based on thermogravimetric analyses (TGA/DTGA). This demonstrates that serpentinization is much faster under alkaline conditions refering to previous study at comparable conditions [35,36,43] and can lead to total replacement of <30µm olivine in less than 30 days and 90 days for 30<particle size<56 µm.

2 Materials and Methods

Millimetric grains of olivine San Carlos (Fo_{90}) were crushed by using a Fritsh Pulverisette 7 micro-crusher. Three classes of grain/particle size (particle size<30µm, 30<particle size<56µm and 56<particle size<150µm) were isolated by sieving. The samples

were washed three times using high-pure water in order to remove the ultrafine particles that possibly stuck at grain surfaces during crushing step. Optical and electron microscopy was performed to control the initial state/appearance of olivine surfaces.

2.1 Alteration experiments

1.5ml of high alkaline solution (1M of NaOH, pH≈13.5 at 25°C) and 100mg of San Carlos olivine at a given class of particle size were placed in a Teflon cell reaction (cap-cell also in Teflon). Cell reaction and cap-cell were previously washed by an acidic treatment followed by washing with high-pure water. This cell reaction was immediately assembled into a steel autoclave without agitation, referred as "static batch reactor" and the closed autoclave was placed in a multi-oven (ten independent-temperature compartments) and heated to 150°C or 200°C (P_{sat}~0.5Mpa and P_{sat}~1.6Mpa). Various olivine-alkaline solution reaction times from 3h to 90 days were considered in order to determine the mineral replacement rate (or serpentinization rate) of olivine at the investigated hydrothermal conditions. Particularly, the effect of initial particle size (three different classes: particle size<30µm, 30<particle size<56µm and 56<particle size<150µm) on the serpentinization rate of olivine was tested. All experimental conditions are summarized in table 1.

At the end of the experiment, the autoclave was quenched in cold water. This manipulation avoids precipitation during cooling with no perturbation of the reaction products. Then, the autoclave was disassembled and the fluid was collected for pH and major elements concentration (Mg, Fe and Si) measurements (not shown in this study). After all experiments, pH of the experimental fluid is still around 13.5 (measured at 25°C). The solid product was dried directly in the Teflon cell at 80°C for 24h. The dry solid product was recovered for further solid characterizations described below.

2.2 X-Ray diffraction measurements

X-Ray diffraction (XRD) analyses were performed in the ISTerre laboratory. All samples were crushed manually. The powders were carefully placed and manually compacted in borosilicated capillaries of 500µm of diameter, this corresponds to about 5 mg of sample. XRD patterns were recorded with a Bruker D8 powder diffractometer equipped with a SolX Si (Li) solid state detector from Baltic Scientific Instruments using CuKα1-Kα2 radiation and a Göbel mirror. Intensities were recorded for an 2θ interval from 5 to 80° with an 8 s counting time per 0.024° 2θ step for bulk mineralogy determination.

2.3 FESEM observations

Grain size and morphology of the experimental products were characterized using secondary or backscattering electrons. Micro-imaging was obtained using Zeiss Ultra 55 Field emission gun scanning electron microscopy (FESEM). This enables a spatial resolution of approximately 1nm at 15 kV. Samples were dispersed by ultrasonic treatment in absolute ethanol for at least 5mn in order to disaggregate the particles. One or two drops of dispersion were placed onto an aluminium support and coated with a thin film of platinium for SEM observation.

2.4 Thermogravimetric analyses (TGA)

TGA for experimental solid products were performed with a TGA/SDTA 851^e Mettler Toledo instrument under the following conditions: sample mass of about 10 mg, platine crucible of 150 µl with a pinhole, heating rate of 10 °C min^{-1}, and inert N_2 atmosphere of 50 ml min^{-1}. Sample mass loss and associated thermal effects were obtained by TGA/DTGA in a temperature range from 30°C to 1200°C. In order to identify the different mass loss steps, the TGA first derivative (rate of mass loss) was used. TGA apparatus was calibrated in terms of mass and temperature. Calcium oxalate was used for the sample mass calibration. The melting points of three compounds (indium, aluminium and copper) obtained from the DTGA signals

were used for the sample temperature calibration. The temperature accuracy of the TGA/SDTA system is about ± 0.25°C. The weighting accuracy is around 0.1µg, which correspond to 0.01% for a 10mg sample.

2.5 FTIR measurements

FTIR measurements (in transmission mode) were performed using an IR microscope Bruker Hyperion 3000. The IR beam was focused through a 15x lens and the typical size of infrared aperture is 50*50 µm². The light source is a Globar(TM) and the beam splitter is in KBr. The spectra were measured from 700 to 4000 cm^{-1} (4cm^{-1}resolution) with a MCT monodetector cooled by liquid nitrogen.

Samples must be thin (less than 100 µm) and flat to avoid absorption band saturation or scattering effects. Sample preparation has involved a careful crushing of samples in mortar and manual compaction of fine crushed particles between two K-Br windows. Five spectra per samples were realized; they were fitted using OPUS software.

3 Results and discussion

3.1 Serpentinization reaction under alkaline conditions

Secondary minerals were identified by XRD and FESEM (Figs. 1 and 2) and they were quantified by TGA (Fig. 3). Under alkaline conditions, olivine is replaced by chrysotile and brucite, independently on the starting grain size of olivine. No other minerals were detected and/or observed during this alteration reaction.

FESEM micro-imaging has revealed a clear evolution of particle size and morphology of crystal faces during serpentinization advancement (Fig. 2). Serpentine nucleation at olivine-alkaline solution interfaces is observable by FESEM after only few hours of reaction when the starting grain size is <30µm (Fig. 2a). These occur as nanosized nodules forming irregular sub-micrometric rods. They are still observed onto olivine surfaces after few days of

reaction and a more advanced serpentinization reaction (Fig. 2c). The irregular sub-micrometric rods were identified as chrysotile and brucite "nucleates" from TGA/DTGA in the solid product (Fig. 3). While brucite is detected by XRD in the first stages of replacement (e.g. 3 hours of reaction for <30µm grains), chrysotile was not detected by XRD , possibly due to its poor crystallinity and/or nanometric size. Chrysotile was detected by XRD after 16h of reaction for the smallest starting grains (<30µm), however, several days of olivine-fluid interactions are required when the starting grain size is >30µm (Fig. 1a, b). At advanced alteration stages, serpentinized samples consist of tubular, conical and cylinder-in-cylinder chrysotile with nanometric diameter and microsized hexagonal brucite were clearly observed (Fig. 2e, g, h). Diameter of secondary products depends of the starting material grain size. It increases from ~50 nm for the <30 µm, to 200-300 nmfor 30-56 µm and 56-150 µm fractions. Lizardite was not observed. Previous study suggested that lizardite crystallized at lower levels of supersaturation than chrysotile [44]. Here, we confirm that high alkaline pH favors chrysotile precipitation [40,42].

In natural samples, olivine replacement in mesh texture is commonly described as an assemblage of serpentine±brucite±magnetite. Typically, the magnetite amount depends on the Mg# (Mg# = Mg / (Mg +Fe)) in primary olivine. Neither iron oxides (ex. magnetite or hematite) nor oxyhydroxides (ex. goethite) were observed in our experiments. Semi-quantitative EDS analyses have revealed that the initial iron contained in olivine was preferentially incorporated as Fe^{2+} into brucite ($Mg\#_{brucite}$=0.84), and slightly sequestered into/onto chrysotile ($Mg\#_{chrysotile}$=0.95) compared to starting San-Carlos olivine. In our conditions a part of Fe^{3+} (not determined) might substitute to Si into the chrysotile. In our experiments, one general reaction of San Carlos olivine alteration can be written as: follows:

$$2Mg_{1,8}Fe_{0,2}SiO_4 + 3H_2O = (Mg_{1-Z}Fe_Z)(OH)_2 + (Mg_{1-X}Fe_X)_3Fe_YSi_{2-Y}(OH)_4 \quad (1)$$

with X+Y ~0.05 and Z~0.16

188 This isochemical reaction implies a volume increase of ~25% (see discussion below).

189 On the XRD patterns (Fig. 1), characteristic peaks of chrysotile appear in the first hours
190 or days of reaction, depending on the initial particle size of olivine (Fig. 1a, b). Secondary
191 product growth rate is related to the variation of the crystal size with time. On the XRD
192 patterns the full width at half maximum (FWHM) parameter for specific peaks, corresponding
193 to a crystalline compound, can be directly associated to its coherent domain size when
194 instrumental resolution function (IRF) and strain contribution are known. In our case, the
195 FWHM for the plane (002) of chrysotile was used to obtain an estimation of the chrysotile
196 size variation during the serpentinization process. Here, a decrease of FWHM implies an
197 increase of coherent domain size as specified in the Scherrer equation. The FWHM variation
198 with the reaction time reported in figure 1c shows a fast crystal growth step followed by a
199 slow crystal growth step for chrysotile from 3h to 30 days when starting grain size is <30µm.
200 Conversely, chrysotile coherent domain varies only moderately from 20 to 90 days for
201 starting grain size > 30 µm (Fig. 1c). In this latter case, two explanations are possible: firstly,
202 a preferential growth of other(s) crystal plane(s) than plane (002) is involved, secondly, a
203 dominant nucleation events promoting an increase of particle number concentration with time
204 during mineral replacement of olivine can occur. FESEM observations support the first
205 assumption because they have revealed a higher radial growth of tubular chrysotile for larger
206 starting grain size (30-56µm and 56-150 µm) at similar reaction time (Fig. 2f, h).

207 ## 3.2 Determination of serpentinization rate

208 The time for complete olivine-to-serpentine transformation or complete
209 serpentinization process depends on the starting grain size. For example, 30 days were
210 required when starting grain size was <30µm while about 90 days were required for the 30-
211 56µm fraction (Fig. 1a, b). For 56-150µm starting grain size, around 55% of mineral
212 replacement was reached after 90 days of experiments.

213 Serpentinization rate of olivine was determined by using a simple and novel method
214 combining TGA and DTGA. TGA/DTGA were performed to quantify the molecular water
215 (adsorbed or confined in pores) and hydroxyl groups (-OH) (incorporated in brucite and
216 chrysotile) as illustrated in figure 3. In general, molecular water (H_2O) adsorbed or confined
217 in pores onto mineral assemblage, was released at moderate temperature (<200°C).
218 Conversely, the brucite and chrysotile minerals were dehydroxylated at higher temperatures.
219 Here, a dehydroxylation peak closed to 370°C was associated to brucite. This peak was
220 shifted towards lower temperature, compared to the dehydroxylation of pure brucite peaking
221 at 430°C. This change of thermal stability was related to a significant incorporated amount of
222 iron (Fe^{2+}) into brucite structure as recently claimed by Okamoto et al. [45]. Additionally we
223 observed that weight loss ratio between serpentine and brucite is not constant following
224 reaction advancement. Regarding the chrysotile, it was observed that it starts to be
225 dehydroxylated at about 400°C and it was completely dehydroxylated at approximately 700°C
226 for most of the experiments. In several cases, two typical dehydroxylation episodes were
227 measured at 515 and 600 °C, respectively. We note that the starting dehydroxylation step for
228 chrysotile can be overlapped with residual –OH from dehydroxylation of brucite, possibly
229 producing a slight over-estimation of incorporated –OH into the chrysotile phase. This direct
230 measurement was used to calculate the serpentinization extent (%) at a given reaction time as
231 follows:
232 $$\xi_t = ((\text{-OH})_{measured}/(\text{-OH})_{theoretical})*100 \quad (2)$$
233 where $(\text{-OH})_{theoretical}$ is the theoretical weigh (in %) of hydroxyl groups incorporated in
234 chrysotile (400°C to 700°C) with a chemical formula simplified to $Mg_3Si_2O_5(OH)_4$ for the (-
235 $OH)_{theoretical}$ considered. Then, the serpetinization extent was correlated with reaction time (ξ_t
236 vs. t). These experimental-calculated data is displayed in figure 3. As previously stated, a
237 complete serpentinization extent was determined after 30 days for smaller olivine grains

(<30μm) and after 90 days for intermediate olivine grains (30<grain size<56). These results clearly show that the serpentinization rate strongly depends on the starting grain size of olivine. This explains why for larger olivine grains (56<grain size<150μm), about 55% of serpertinization extent was only reached after 90 days of olivine-fluid interactions.

Experimental data reported in figure 4 were fitted by using a kinetic pseudo-second-order model. This simple kinetic model describes a fast serpentinization step followed by a slow serpentinization step until an asymptotic maximum with time. Its integrated form can be expressed as follows:

$$\xi_t = \frac{\xi_{max} t}{t_{1/2} + t} \quad (3)$$

where ξ_t, is the serpentinization extent for a given reaction time t; ξ_{max} , the maximum serpentinization extent (close to 100% for a complete serpentinization) and $t_{1/2}$ the half serpentinization time. The fast serpentinization step can be associated to the fast dissolution of smaller olivine grains initially far from equilibrium, but the dissolution process was spatially and temporally coupled to a fast precipitation of chrysotile and brucite. For this reason, the external shape of starting olivine grains (primary or parent mineral) was preserved, leading to a porous granular material composed of chrysotile and brucite minerals when complete mineral replacement of olivine was reached. Finally, the mineral replacement initial-rate v_0 (or serpentinization initial-rate) was defined as the slope of the tangent line when time t tends toward zero on the r vs t curve. Analytically, $v_0=(\xi_{max}/t_{1/2})$ and it varies from 3.6×10^{-6} s^{-1} to 1.4×10^{-7} s^{-1} respectively for <30μm grain size and 56-150μm grain size. Full serpentinization was not obtain experimentally on 56<particle size<150 μm but the theoretical model presented predict a close to complete serpentinization (>90%) around 2 years.

Indeed, the fluid/olivine interface depending of the initial olivine grain size is the main factor controlling the initial rate. These kinetic parameters concerning the three different size classes of olivine and respective correlation factors are summarized in table 2.

The uncertainties of the TG-method result from the calculation method. The main approximation is the systematic consideration of the same temperature range (400-700°C). Refering to all the experiments, a variation of the temperature range of ± 50°C will only induce a difference of 1- 5% for the final serpentinization advancement calculated. Based on this calculation we assure that the maximum uncertainty of the proposed methods is around 5% as reported in figure 4. The uncertainty on the calculated initial rate is directly depending on the standard deviation obtained for $t_{1/2}$ and ξ_{max} (Table 2).

In a complementary way, the transmission FTIR spectra were obtained. Characteristic stretching bands for hydroxyl group (-OH) in chrysotile-brucite and for Si-O group in olivine-chrysotile were used. Particularly, the relative (-OH)/(Si-O) ratio using integrated bands intensities or maximum band intensities was correlated with the serpentinization extent deduced from TG/DTG analyses (Fig. 5). This gives two calibration curves that can be used to determine serpentinization rate using FTIR measurements. However, FTIR measurements should be taken with caution because of the overlapping of –OH (for brucite and serpentine) and Si-O groups (for serpentine and olivine). We could overcome this problem if serpentine/brucite produced molar ratio stayed constant following reaction time, but as described before it is not the case. Here, we conclude that the TG/DTG analyses are a powerful tool to determine the mineral replacement rate of olivine by chrysotile-brucite mineral assemblage. For this specific case, the FTIR measurements provide a first information about the olivine serpentinization extent.

This study confirms that the serpentinization rate is enhanced by high alkaline conditions. Serpentinisation rate has been studied for a large variety of experimental

conditions under neutral conditions [33–40,46]. For comparison, serpentinization extent of 50-100 μm starting grain size at 200°C reached only ~20% after ~4 months under neutral conditions (Seyfried et al., 2007). This corresponds to a kinetic 5 times slower to our results on the largest starting grain size (56-150 μm).

3.3 Serpentinization steps and reaction mechanism

Contemporaneously, the first steps of reaction in alkaline medium are characterized by a fast dissolution of olivine associated to the formation of preferential dissolution figures as notches and etch pits (Fig. 6a, b, c) [44–46]. Conjointly, precipitation of the first nucleates of brucite and chrysotile occur at the olivine surface. FESEM observations have revealed the preservation of olivine shape after complete serpentinization (Fig. 7). This suggests that olivine alteration invokes coupled dissolution-precipitation processes [28]. Despite ultrasonic treatment and dispersion on ethanol (up to 1h30), which can easily break up the new brucite/chrysotile mineral assemblage, the shape and size of olivine grains are always preserved regardless the completion of the reaction. The few scattered chrysotile grains observed are the result of tearing from olivine grain surfaces and are not the result of precipitation from saturated solution away from olivine grain. Based on these results, we assume a higher super-saturation of solution with respect to chrysotile tubes at the olivine-solution interfaces. Supersaturation at olivine-alkaline solution interfaces allows rapid heterogeneous serpentine nucleation as small nodules of chrysotile and brucite (Fig. 2a). This nucleation phase is followed by a phase of epitaxial growth of chrysotile and brucite forming a porous medium (Fig. 6d, e, f). Chrysotile grows as elongated tubes with various morphology (conical, cylinder in cylinder) with a size depending on starting olivine grain size. Largest starting grain size induces smallest reacting surface and thus slower kinetic of alteration and formation of largest chrysotiles particles. Olivine grain size influenced initial dissolution rate v_0, passivation state and general kinetic of alteration.

Serpentinization reaction is then favored by the formation of notches connected to a micro-fracturing network inside olivine (e.g. 32 days of reaction for >30 μm grains; Fig. 6b, c). This micro-fracturing network might start following ordered families of fine-scale fractures from olivine grains [44]. In the oceanic crust, the microfracturing may be attributed to the stress generated by the volume increase during olivine serpentinization [28]. In our free fluid system, there is no evident expansion during olivine replacement. Volume increase due to olivine serpentinization (25%) is likely accounted by material loss in solution, but it could also cause the microfracturing [28,50]. With the formation of smaller sub-grains, microfracturing allows an easier fluid percolation and increase the total reaction-surface (Fig. 6e, f). This process permits a continuous and total replacement of olivine by chrysotile and brucite as summarized in figure 8. This is in agreement with natural observation and development of mesh type texture described in natural rocks [26–28,50–52]. Fluid can percolate everywhere without formation of a passivation layer at grain surface. The formation of a protective layer would induce a non-continuous passivation process by blocking intra-particles diffusion [53]. Mass transfer will play a major role for the preservation of volume and shape of starting olivine grain.

4 Conclusion

Olivine alteration was investigated under alkaline conditions for different starting grain sizes at 200 °C. In this study, we were able to follow complete olivine replacement by an assemblage of chrysotile and brucite.

Thermogravimetric analyses were used to investigate the dehydroxylation of hydrated phases and thus the serpentinization extent as a function of time. Based on this innovative approach, we were able to estimate punctually the serpentinization advancement and a kinetic

pseudo-second-order model was used to describe experimental data. This could allow a prediction of reaction advancement for the largest starting grain size.

We also established two calibration curves between the -OH/Si-O bands measured in FTIR and the degree of serpentinization. This enables to have an estimation of the kinetic rates of serpentinization directly from the FTIR spectra analysis. This must be considered with caution because of the overlapping of –OH bands between brucite and serpentine.

Under our experimental conditions, olivine is replaced by chrysotile and brucite by coupled dissolution-precipitation processes. Fast dissolution of olivine, preferential dissolution features formation and process of grain subdivisions by fracturing are involved to explain a complete mineral replacement of olivine. This implies the preservation of external shape of olivine grains as typically observed in natural systems.

Acknowleggements

The authors are grateful to French National Center for Scientific Research (CNRS and University Joseph Fourier (UJF) in Grenoble for providing the financial support. R. Lafay was supported by a Ph.D grant from French education ministry. The authors are grateful to IPAG institute where infrared measurements where performed.

References:

[1] F. Deschamps, S. Guillot, M. Godard, C. Chauvel, M. Andreani, K. Hattori, In situ characterization of serpentinites from forearc mantle wedges: Timing of serpentinization and behavior of fluid-mobile elements in subduction zones, Chemical Geology. 269 (2010) 262–277.

[2] K. Hattori, S. Guillot, Volcanic fronts form as a consequence of serpentinite dehydration in the forearc mantle wedge, Geology. 31 (2003) 525–528.

[3] K. Hattori, S. Guillot, Geochemical character of serpentinites associated with high- to ultrahigh-pressure metamorphic rocks in the Alps, Cuba, and the Himalayas: Recycling of elements in subduction zones, Geochemistry Geophysics Geosystems. 8 (2007).

[4] C.-T.A. Lee, M. Oka, P. Luffi, A. Agranier, Internal distribution of Li and B in serpentinites from the Feather River Ophiolite, California, based on laser ablation inductively coupled plasma mass spectrometry, Geochem. Geophys. Geosyst. 9 (2008) Q12011.

[5] T.M. McCollom, E.L. Shock, Fluid-rock interactions in the lower oceanic crust: Thermodynamic models of hydrothermal alteration, J. Geophys. Res. 103 (1998) 547–575.

[6] F. Vils, L. Pelletier, A. Kalt, O. Müntener, T. Ludwig, The Lithium, Boron and Beryllium content of serpentinized peridotites from ODP Leg 209 (Sites 1272A and 1274A): Implications for lithium and boron budgets of oceanic lithosphere, Geochimica et Cosmochimica Acta. 72 (2008) 5475–5504.

[7] F. Deschamps, S. Guillot, M. Godard, M. Andreani, K. Hattori, Serpenttines act as sponges for Fluid-Mobile-Elements in abyssal and subduction zone environments, Terra Nova. 23 (2011) 171–178.

[8] S. Guillot, K.H. Hattori, J. de Sigoyer, T. Nagler, A.-L. Auzende, Evidence of hydration of the mantle wedge and its role in the exhumation of eclogites, Earth and Planetary Science Letters. 193 (2001) 115–127.

[9] A. Bloise, E. Belluso, E. Fornero, C. Rinaudo, E. Barrese, S. Capella, Influence of synthesis conditions on growth of Ni-doped chrysotile, Microporous and Mesoporous Materials. 132 (2010) 239–245.

[10] A. Bloise, E. Belluso, E. Barrese, D. Miriello, C. Apollaro, Synthesis of Fe-doped chrysotile and characterization of the resulting chrysotile fibers, Cryst. Res. Technol. 44 (2009) 590–596.

[11] A.B. Bloise, Hydrothermal alteration of Ti-doped forsterite to chrysotile and characterization of the resulting chrysotile fibers, njma. 185 (2009) 297–304.

[12] E. Korytkova, L. Pivovarova, V. Gusarov, Influence of iron on the kinetics of formation of chrysotile nanotubes of composition $(Mg, Fe)_3Si_2O_5(OH)_4$ under hydrothermal conditions, Geochemistry International. 45 (2007) 825–831.

[13] A. McDonald, B. Scott, G. Villemure, Hydrothermal preparation of nanotubular particles of a 1:1 nickel phyllosilicate, Microporous and Mesoporous Materials. 120 (2009) 263–266.

[14] B. Wunder, F. Deschamps, A. Watenphul, S. Guillot, A. Meixner, R. Romer, et al., The effect of chrysotile nanotubes on the serpentine-fluid Li-isotopic fractionation, Contributions to Mineralogy and Petrology. 159 (2010) 781–790.

[15] G. Falini, E. Foresti, I.G. Lesci, B. Lunelli, P. Sabatino, N. Roveri, Interaction of Bovine Serum Albumin with Chrysotile: Spectroscopic and Morphological Studies, Chem. Eur. J. 12 (2006) 1968–1974.

[16] A.F. Gualtieri, M.L. Gualtieri, M. Tonelli, In situ ESEM study of the thermal decomposition of chrysotile asbestos in view of safe recycling of the transformation product, Journal of Hazardous Materials. 156 (2008) 260–266.

[17] E. Foresti, E. Fornero, I.G. Lesci, C. Rinaudo, T. Zuccheri, N. Roveri, Asbestos

403 health hazard: A spectroscopic study of synthetic geoinspired Fe-doped chrysotile, Journal of
404 Hazardous Materials. 167 (2009) 1070–1079.
405 [18] P. Sabatino, L. Casella, A. Granata, M. Iafisco, I.G. Lesci, E. Monzani, et al.,
406 Synthetic chrysotile nanocrystals as a reference standard to investigate surface-induced serum
407 albumin structural modifications, Journal of Colloid and Interface Science. 314 (2007) 389–
408 397.
409 [19] A. Beinlich, H. Austrheim, J. Glodny, M. Erambert, T.B. Andersen, CO2
410 sequestration and extreme Mg depletion in serpentinized peridotite clasts from the Devonian
411 Solund basin, SW-Norway, Geochimica et Cosmochimica Acta. 74 (2010) 6935–6964.
412 [20] F. Larachi, I. Daldoul, G. Beaudoin, Fixation of CO2 by chrysotile in low-pressure
413 dry and moist carbonation: Ex-situ and in-situ characterizations, Geochimica et
414 Cosmochimica Acta. 74 (2010) 3051–3075.
415 [21] T.M. McCollom, J.S. Seewald, A reassessment of the potential for reduction of
416 dissolved CO2 to hydrocarbons during serpentinization of olivine, Geochimica et
417 Cosmochimica Acta. 65 (2001) 3769–3778.
418 [22] T. Yajima, T. Ohsumi, Y. Mizuochi, A. Ninomiya, T. Kato, - Field study on CO2
419 fixation by serpentinite rock-bed, dans: Greenhouse Gas Control Technologies 7, Elsevier
420 Science Ltd, Oxford, 2005: p. 2027–2030.
421 [23] P. Beck, E. Quirico, G. Montes-Hernandez, L. Bonal, J. Bollard, F.-R. Orthous-
422 Daunay, et al., Hydrous mineralogy of CM and CI chondrites from infrared spectroscopy and
423 their relationship with low albedo asteroids, Geochimica et Cosmochimica Acta. 74 (2010)
424 4881–4892.
425 [24] M. Andreani, A. Baronnet, A.-M. Boullier, J.-P. Gratier, A microstructural study of a
426 « crack-seal » type serpentine vein using SEM and TEM techniques, European Journal of
427 Mineralogy. 16 (2004) 585 –595.
428 [25] M. Andreani, C. Mével, A.-M. Boullier, J. Escartin, Dynamic control on serpentine
429 crystallization in veins: Constraints on hydration processes in oceanic peridotites, Geochem.
430 Geophys. Geosyst. 8 (2007) Q02012.
431 [26] F.J. Wicks, E.J.W. Whittaker, Serpentine textures and serpentinization, Canadian
432 Mineralogist. 15 (1977) 459–488.
433 [27] B.. Evans, The serpentinite multisystem revisited: Chrysotile is metastable,
434 international Geology review. 46 (2004) 479–506.
435 [28] A. Putnis, Mineral Replacement Reactions, Reviews in Mineralogy and
436 Geochemistry. 70 (2009) 87–124.
437 [29] A. Putnis, C.V. Putnis, The mechanism of reequilibration of solids in the presence of
438 a fluid phase, Journal of Solid State Chemistry. 180 (2007) 1783–1786.
439 [30] Putnis A., Mineral replacement reactions: from macroscopic observations to
440 microscopic mechanisms, Mineralogical Magazine. 66 (2002) 689–708.
441 [31] D.S. Kelley, J.A. Karson, D.K. Blackman, G.L. Fruh-Green, D.A. Butterfield, M.D.
442 Lilley, et al., An off-axis hydrothermal vent field near the Mid-Atlantic Ridge at 30[deg] N,
443 Nature. 412 (2001) 145–149.
444 [32] K.A. Ludwig, D.S. Kelley, D.A. Butterfield, B.K. Nelson, G. Früh-Green, Formation
445 and evolution of carbonate chimneys at the Lost City Hydrothermal Field, Geochimica et
446 Cosmochimica Acta. 70 (2006) 3625–3645.
447 [33] D.E. Allen, W.E. Seyfried, Compositional controls on vent fluids from ultramafic-
448 hosted hydrothermal systems at mid-ocean ridges: An experimental study at 400°C, 500 bars,
449 Geochimica et Cosmochimica Acta. 67 (2003) 1531–1542.
450 [34] A.H. Macdonald, W.S. Fyfe, Rate of serpentinization in seafloor environments,
451 Tectonophysics. 116 (1985) 123–135.
452 [35] C. Marcaillou, M. Muñoz, O. Vidal, T. Parra, M. Harfouche, Mineralogical evidence

453 for H2 degassing during serpentinization at 300 °C/300 bar, Earth and Planetary Science
454 Letters. 303 (2011) 281–290.
455 [36] B. Martin, W.S. Fyfe, Some experimental and theoretical observations on the kinetics
456 of hydration reactions with particular reference to serpentinization, Chemical Geology. 6
457 (1970) 185–202.
458 [37] W.E. Seyfried Jr, W.E. Dibble Jr, Seawater-peridotite interaction at 300°C and 500
459 bars: implications for the origin of oceanic serpentinites, Geochimica et Cosmochimica Acta.
460 44 (1980) 309–321.
461 [38] W.E. Seyfried Jr., D.I. Foustoukos, Q. Fu, Redox evolution and mass transfer during
462 serpentinization: An experimental and theoretical study at 200 °C, 500 bar with implications
463 for ultramafic-hosted hydrothermal systems at Mid-Ocean Ridges, Geochimica et
464 Cosmochimica Acta. 71 (2007) 3872–3886.
465 [39] W.W. Wegner, W.G. Ernst, Experimentally determined hydration and dehydration
466 reaction rates in the system MgO–SiO2–H2O, American Journal of Science. 283A (1983)
467 151–180.
468 [40] K. Yada, K. Iishi, Growth and microstructure of synthetic chrysotile, American
469 Mineralogist. 62 (1977) 958–965.
470 [41] A. Baronnet, B. Devouard, Topology and crystal growth of natural chrysotile and
471 polygonal serpentine, Journal of Crystal Growth. 166 (1996) 952–960.
472 [42] K. Yada, K. Iishi, Serpentine minerals hydrothermally synthesized and their
473 microstructures, Journal of Crystal Growth. 24-25 (1974) 627–630.
474 [43] W.E. Seyfried Jr., D.I. Foustoukos, Q. Fu, Redox evolution and mass transfer during
475 serpentinization: An experimental and theoretical study at 200 °C, 500 bar with implications
476 for ultramafic-hosted hydrothermal systems at Mid-Ocean Ridges, Geochimica et
477 Cosmochimica Acta. 71 (2007) 3872–3886.
478 [44] C. Normand, A.E. Williams-Jones, R.F. Martin, H. Vali, Hydrothermal alteration of
479 olivine in a flow-through autoclave: Nucleation and growth of serpentine phases, American
480 Mineralogist. 87 1699 –1709.
481 [45] A. Okamoto, Y. Ogasawara, Y. Ogawa, N. Tsuchiya, Progress of hydration reactions
482 in olivine–H2O and orthopyroxenite–H2O systems at 250 °C and vapor-saturated pressure,
483 Chemical Geology. 289 (2011) 245–255.
484 [46] M. Bentabol, M.D. Ruiz Cruz, F.J. Huertas, Hydrothermal synthesis (200°C) of Co-
485 kaolinite and Al-Co-serpentine, Applied Clay Science. 42 (2009) 649–656.
486 [47] J. Hövelmann, H. Austrheim, A. Beinlich, I. Anne Munz, Experimental study of the
487 carbonation of partially serpentinized and weathered peridotites, Geochimica et
488 Cosmochimica Acta. 75 (2011) 6760–6779.
489 [48] A. Awad, A.F. Koster van Groos, S. Guggenheim, Forsteritic olivine: effect of
490 crystallographic direction on dissolution kinetics, Geochimica et Cosmochimica Acta. 64
491 (2000) 1765–1772.
492 [49] M.A. Velbel, J.M. Ranck, Etch pits on naturally altered olivine from dunites of the
493 Appalachian Blue Ridge Mountains, North Carolina, USA, Mineral Mag. 72 (2008) 145–148.
494 [50] A. Putnis, H. Austrheim, Fluid-induced processes: metasomatism and metamorphism,
495 Geofluids. 10 (2010) 254–269.
496 [51] F.J. Wicks, E.J.W. Whittaker, J. Zussman, An idealized model for serpentine textures
497 after olivine, The Canadian Mineralogist. 15 (1977) 446 –458.
498 [52] J.B. Moody, Serpentinization: a review, Lithos. 9 (1976) 125–138.
499 [53] G. Montes-Hernandez, A. Pommerol, F. Renard, P. Beck, E. Quirico, O. Brissaud, In
500 situ kinetic measurements of gas–solid carbonation of Ca(OH)2 by using an infrared
501 microscope coupled to a reaction cell, Chemical Engineering Journal. 161 (2010) 250–256.
502
503

Figure Captions:

Table 1: Summary of the experimental conditions.

Table 2: Summary of kinetic parameters obtained from the pseudo-second-order model.

Figure 1: XRD patterns following reaction advancement, a) with starting grain size <30µm, b) with starting grain size 30-56 µm, c) example of plot for the peak corresponding to bragg angle (2θ) of 12.1° and miller indice (002) with a gaussian deconvolution and plot of FWHM following reaction time for this peak. O: olivine, B: Brucite and S: serpentine.

Figure 2: Scanning electron microscope imaging of the experimental products. All shown experiments have been performed at pH=13.5 (at 25°C) and 200°C, for <30 µm (a, b, c and e), 30-56 µm (d, f, g) and 56-150µm (h) grains size. a) chrysotile and brucite nodules after 3hours of reaction (run no.1), b) chrysotile tube after 30 days of reaction (run 8) and c) nodules aggregated in a tubular shape after 3 days of reaction (run no.5), d) chrysotiles "bunch" at olivine grain surface after 10 days of reaction (run no.13), e) characteristic brucite/chrysotile assemblage after 30 days of reaction (run no.6), f,g) characteristic brucite/chrysotile assemblage and thick cylinder-in cylinder chrysotile after 90 days of reaction (run no.18), and h) characteristic brucite/chrysotile assemblage after 32 days of reaction (run no.20). Bru: brucite, Ctl: chrysotile, Ol: olivine.

Figure 3: a) Thermogravimetric analyses (TGA) for experiments of 3 hours to 30 days (run no. 1,3,5,6,7and 8) with fraction grains <30 µm, b) focus and decomposition of TGA and DTG corresponding spectra after 10 days of reaction.

Figure 4: Serpentinization degree versus time for the hydration reaction at different grain sizes for T=200°C, P_{sat}=1.6Mpa and fluid/solid=15. Maximum error bars corresponding to 5% of the serpentinization extent calculated was also reported. Data were fitted by using a kinetic pseudo-second-order model.

Figure 5: a) Transmission spectra (in absorbance) for starting grain size <30μm after 3 hour (run no.1) and 30 days (run no.8) of reaction with corresponding base line and range employed for treatment. Blue area correspond to -OH band integration A1 with maximum intensity I1, green area correspond to Si-O band integration A2 with maximum intensity I2, b) corresponding -OH/Si-O ratio: A1/A2 and I1/I2 following serpentinization advancement determined by TG and DTG analysis, square, triangle and circles correspond respectively to experiments for <30μm, 30-56μm and 56-150 μm starting grain size fraction (empty for A1/A2 and black for I1/I2) with corresponding standard deviation corresponding, black line correspond to best linear regression with the exclusion of red point.

Figure 6: Scanning electron microscope imaging of the experimental products for starting grain size <30 μm (a), 30-56 μm (c-f) and 56-150 μm (b). a) etch pits at olivine grain surface after 3 days (run no.5), b) dissolution notches after 32 days of reaction (run no. 20), c) dissolution notches after 24 days of reaction (run no. 14), d) chrysotile micro-tubes at olivine grain surface after 3 days of reaction (run no.12), e) contact between two olivine grains and f) microfracturing in section after 10 days of reaction (run no.13). Red dotted lines represent initial border of the supposed crack. Ctl: chrysotile, Ol: olivine.

550 Figure 7: XRD pattern and corresponding scanning electron microphotography from pure
551 starting San Carlos olivine to close to 100% of replacement by serpentine and brucite. Note
552 the preservation of the olivine grains dimension and shape. S: serpentine, B: brucite, O:
553 olivine.

554 Figure 8: Schematic synthesis presenting the different steps of olivine replacement by
555 chrysotile and brucite.

556 Table 1

Run no.	T (°C)	Time	grain size (µm)	Olivine to Chrysotile conversion (%)	products starting-material
1	200	3 h	<30 µm	10.3	O>C>B
2	200	16 h	<30 µm	21.7	O>C>B
3	200	24 h	<30 µm	24.6	O>C>B
4	200	48 h	<30 µm	37.5	O>C>B
5	200	72 h	<30 µm	51.7	O≈C>B
6	200	10 day	<30 µm	73.8	C>O>B
7	200	20 day	<30 µm	88.8	C>B>O
8	200	30 day	<30 µm	98.0	C>B
9	200	90 day	<30 µm	98.2	C>B
10	150	30 day	<30 µm	49.5	O≈C>B
11	150	66 day	<30 µm	not determined	C>O>B
12	200	3day	30-56 µm	19.6	O>C>B
13	200	10 day	30-56 µm	26.2	O>C>B
14	200	24 day	30-56 µm	46.2	O≈C>B
15	200	41 day	30-56 µm	77.1	C>O>B
16	200	51 day	30-56 µm	71.1	C>O>B
17	200	72 day	30-56 µm	88.9	C>B>O
18	200	90 day	30-56 µm	94.4	C>B>O
19	200	13 day	56-150 µm	10.7	O>C>B
20	200	32 day	56-150 µm	26.6	O>C>B
21	200	60 day	56-150 µm	44.2	O>C>B
22	200	90 day	56-150 µm	55.4	C>O>B

557 All experiments have been performed at pH 13.5 (measured at 25°C). Saturated pressure is
558 constant: 1.6MPa for 200°C and 0.5 MPa for 150°C reactions. Fluid/rock ratio is always ~15.
559 O: olivine, C: chrysotile, B: brucite.

560 Table 2

Initial particule size of olivine	Smax (%)		$t_{½}$ (days)	Initial rate (1/s)	fitting r^2
	Exp.	Calc.			
<30 µm	97.96	100±1.7	3.2±0.3	3.62-06±0.35E-06	0.989
30-56 µm	94.35	100±8.5	23.1±5.3	5.01E-07±0.9E-07	0.947
56-150 µm	55.4	100±16	79±21	1.46E-07±0.2E-07	0.981

561

562

563 Figure 1

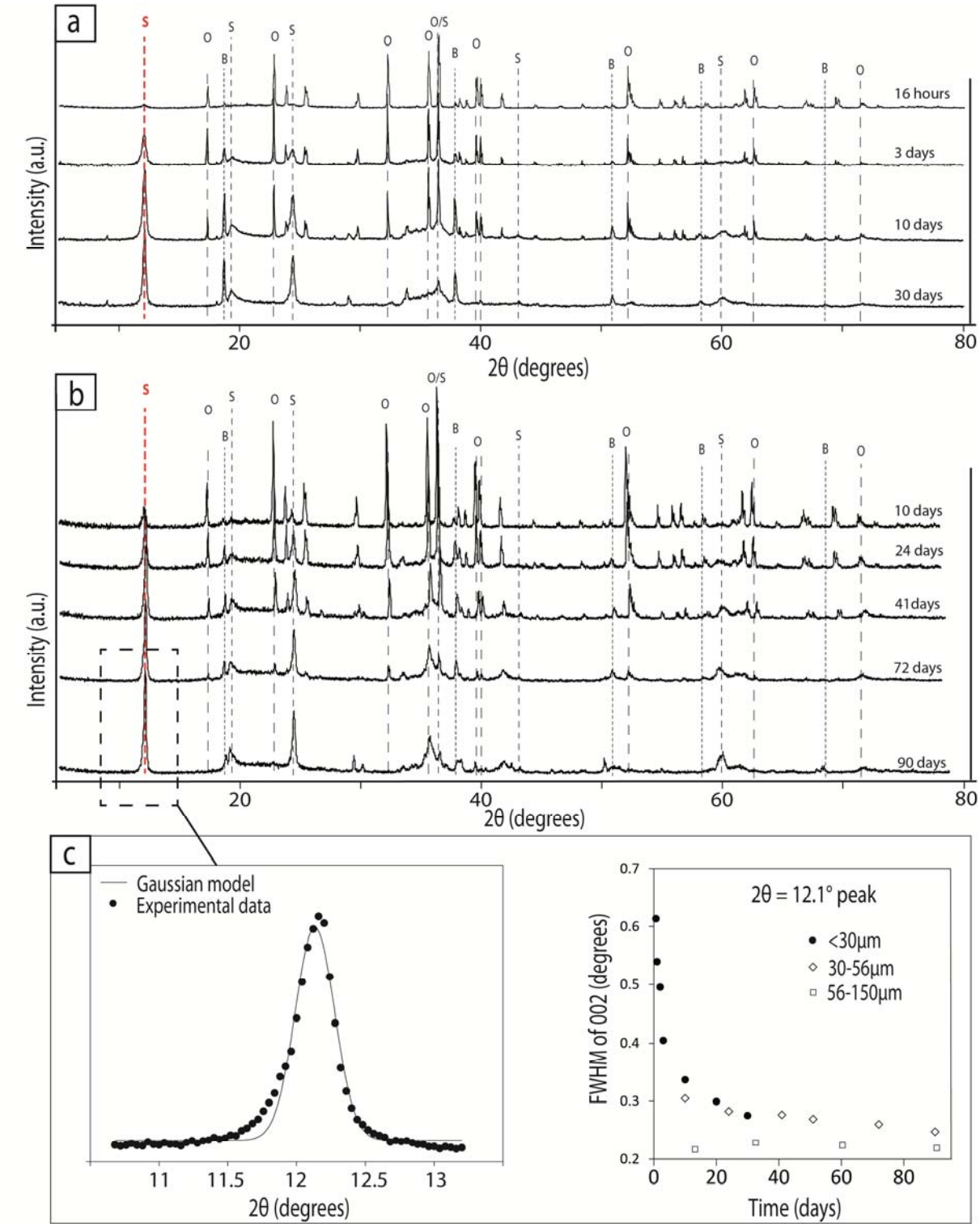

564

565 Figure 2

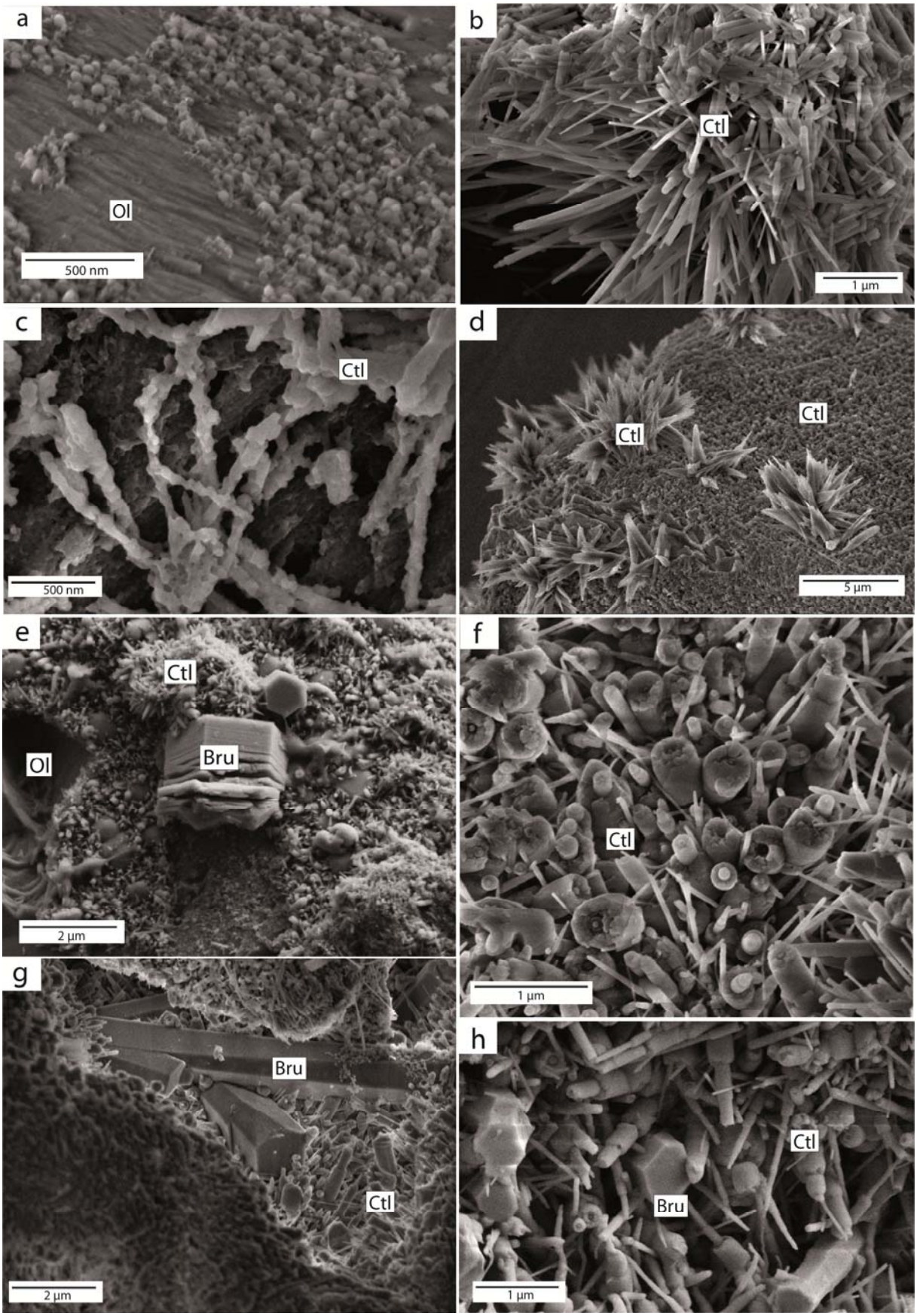

566

567 Figure 3

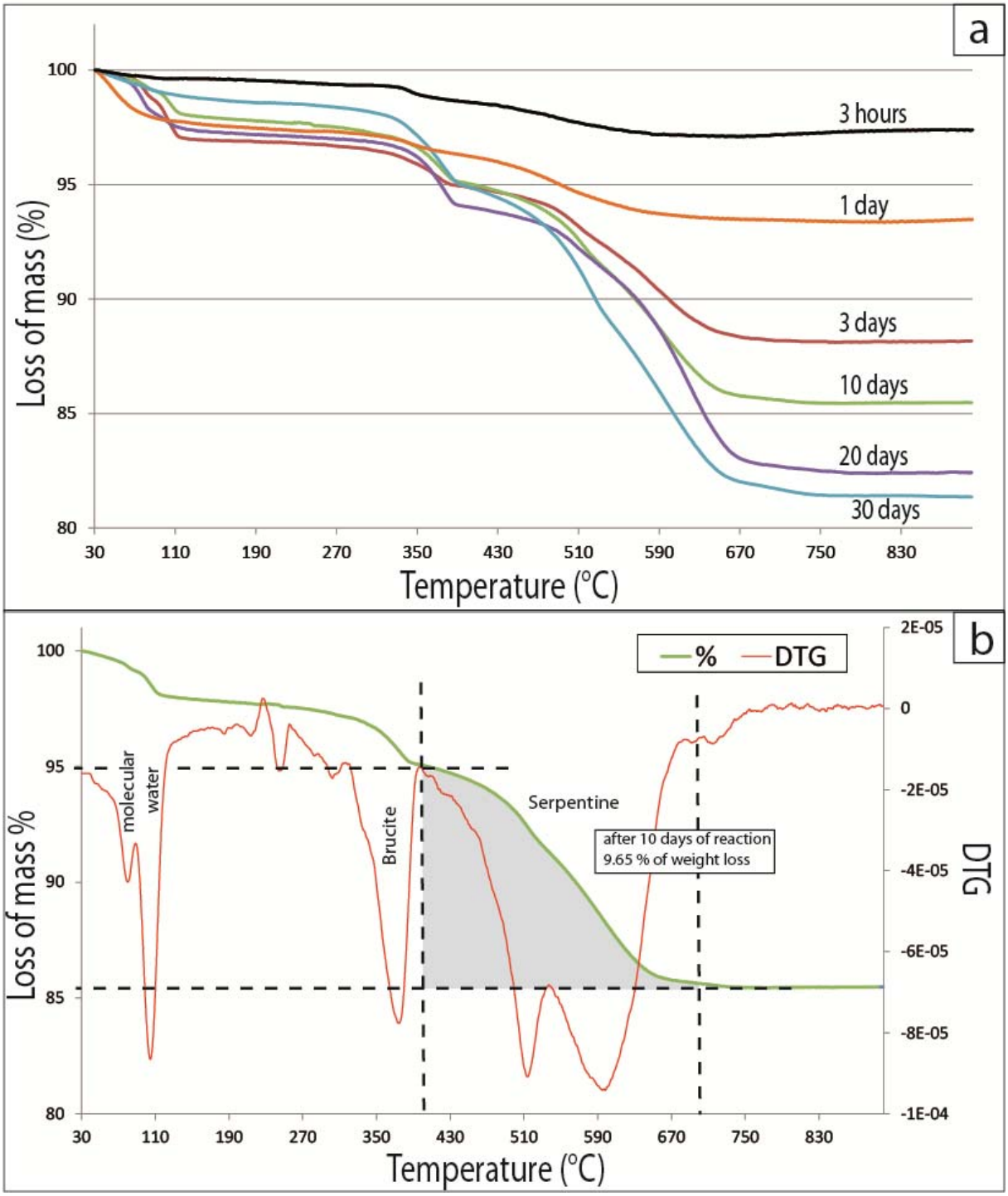

568

569 Figure 4

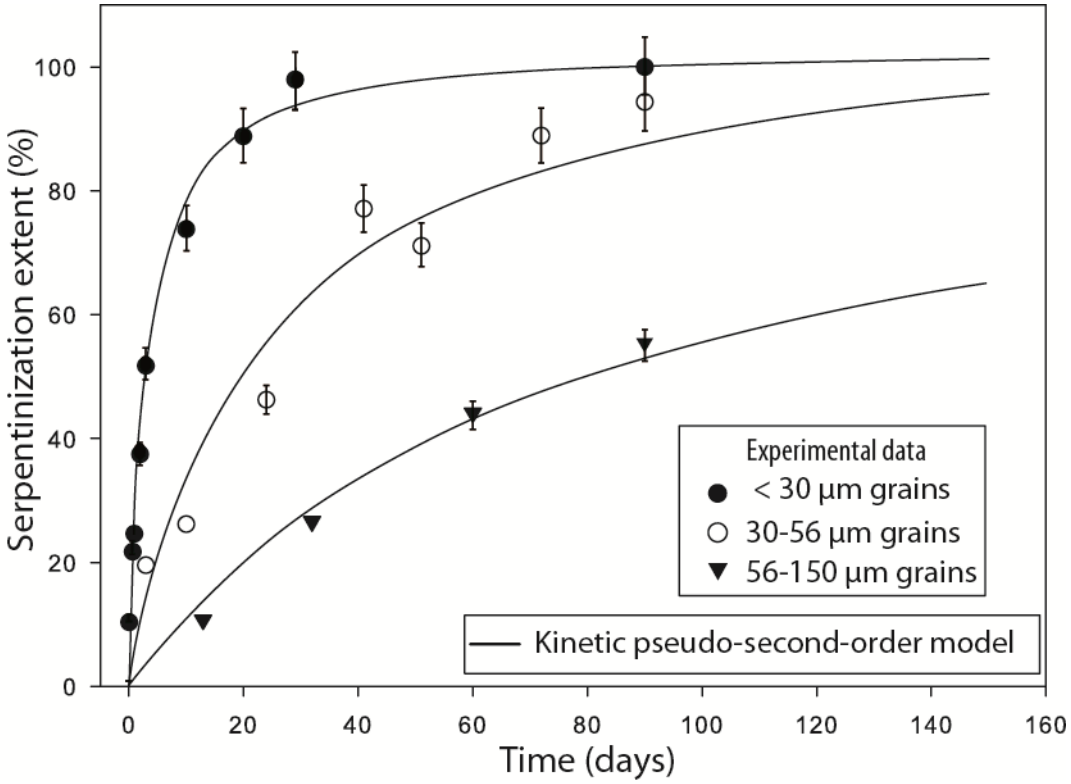

570

571 Figure 5

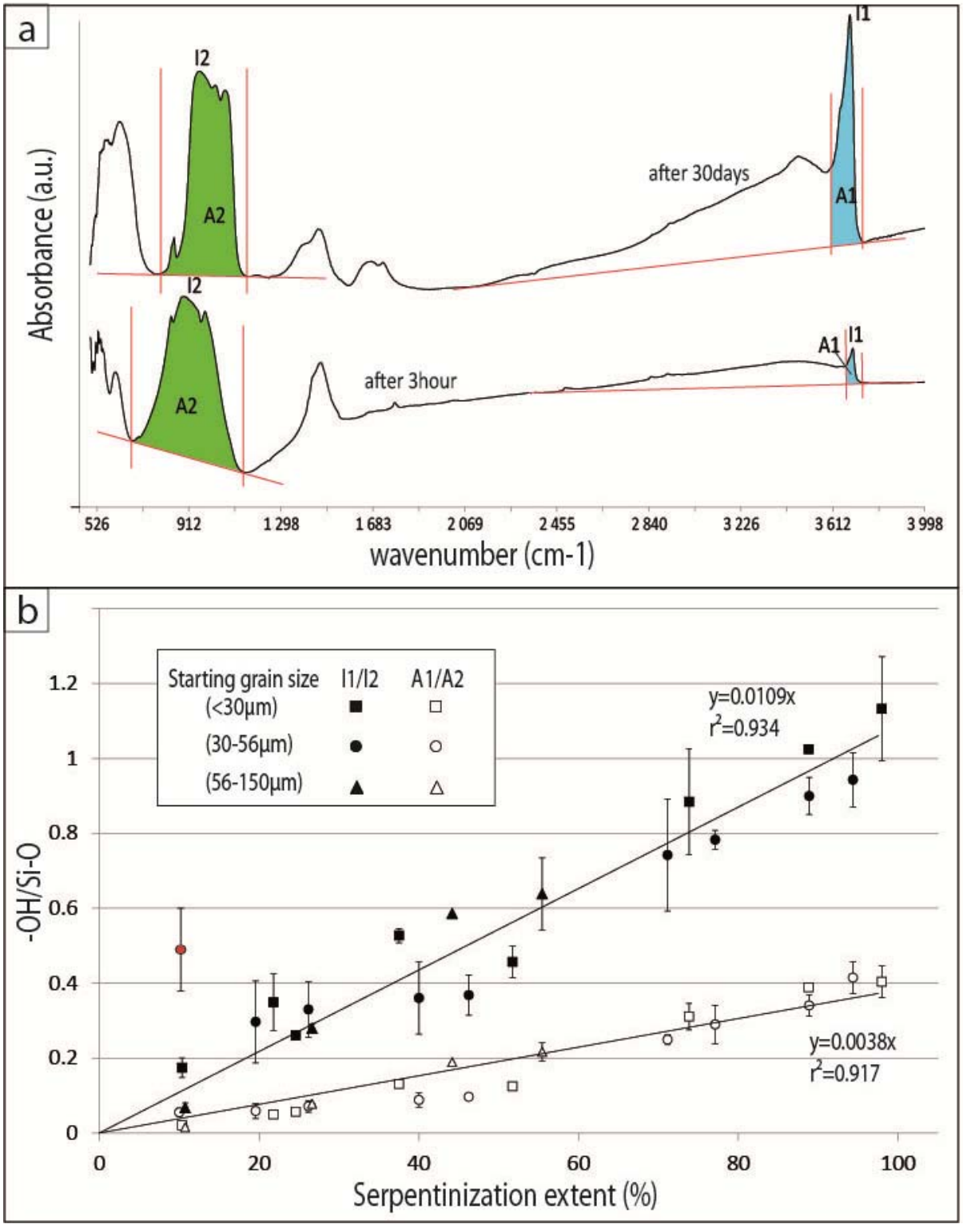

572

573

574 Figure 6
575

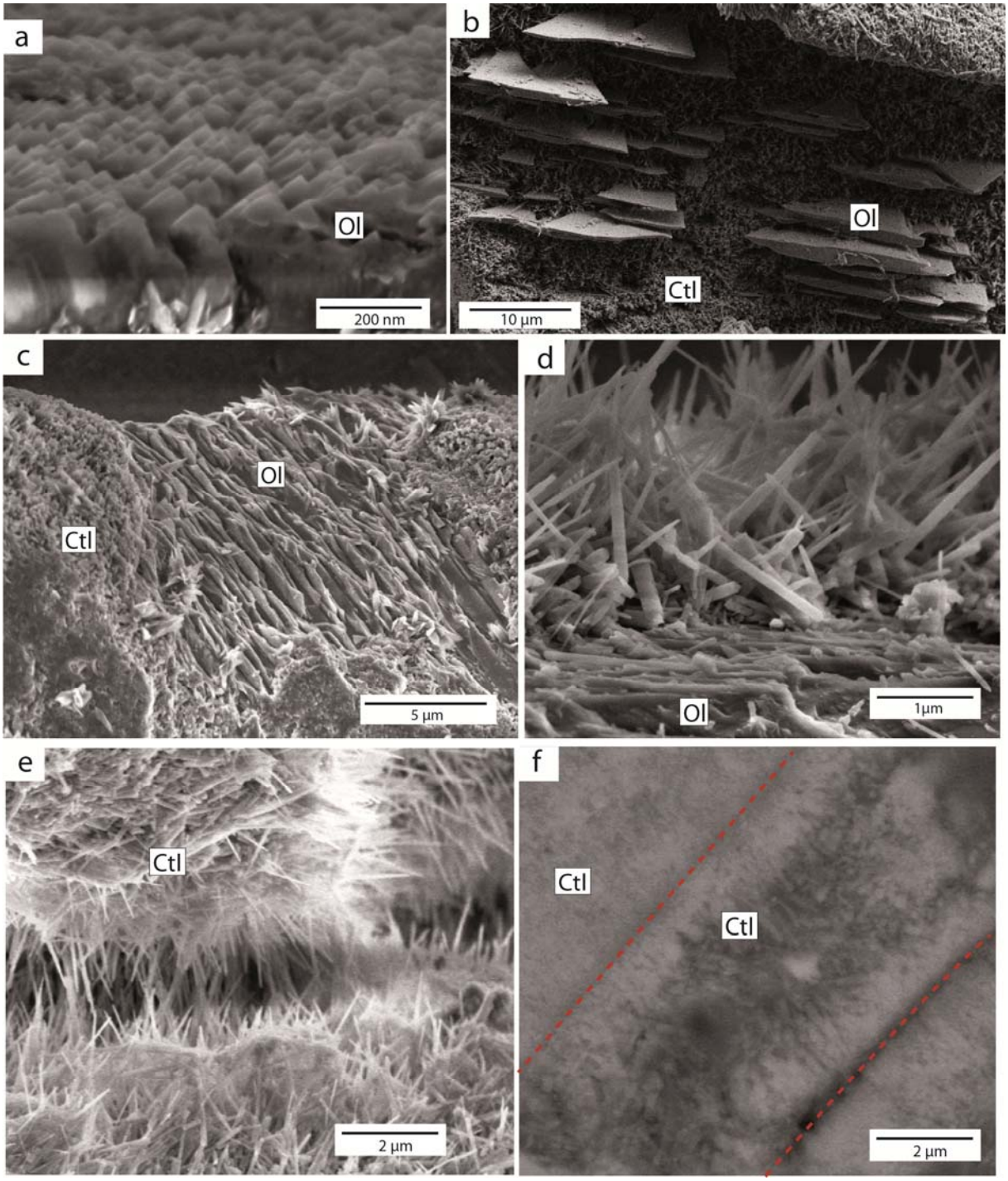

576
577

578

579 Figure 7

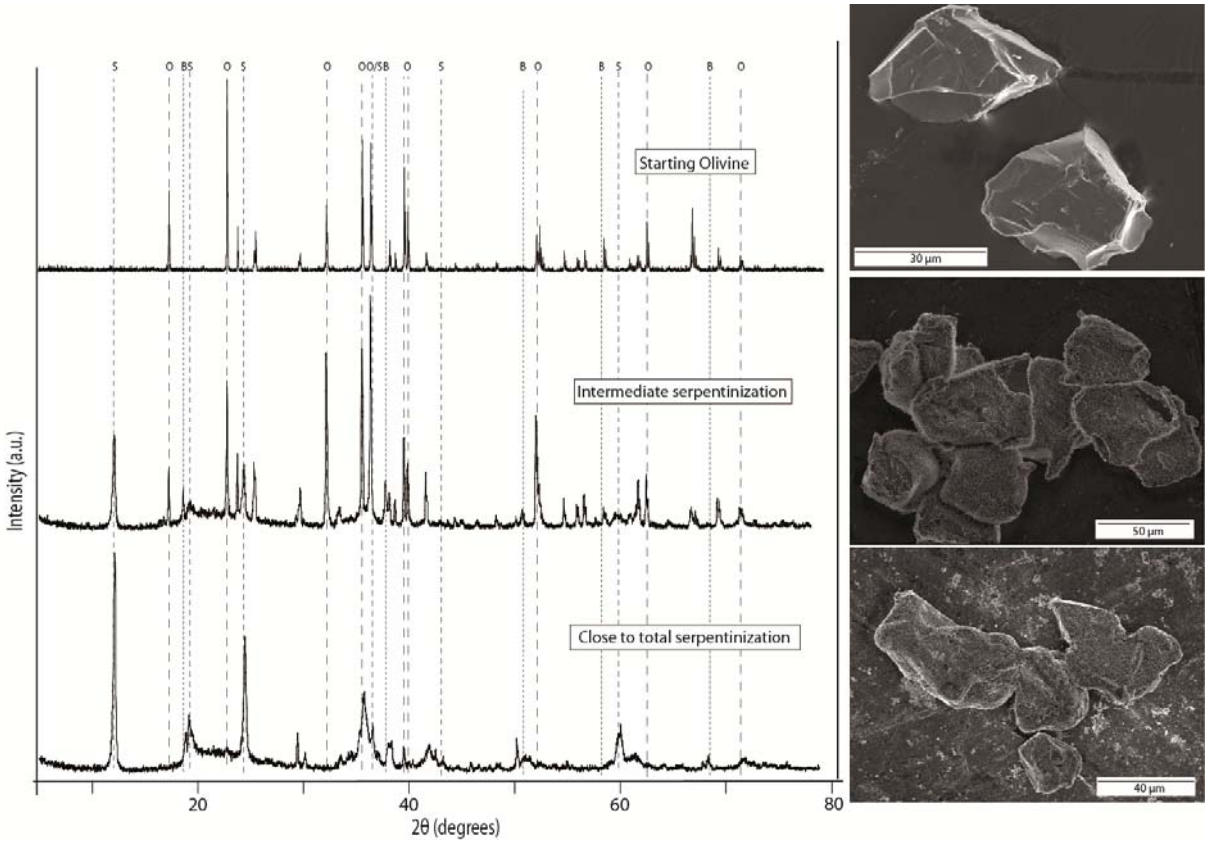

580

581

582 Figure 8

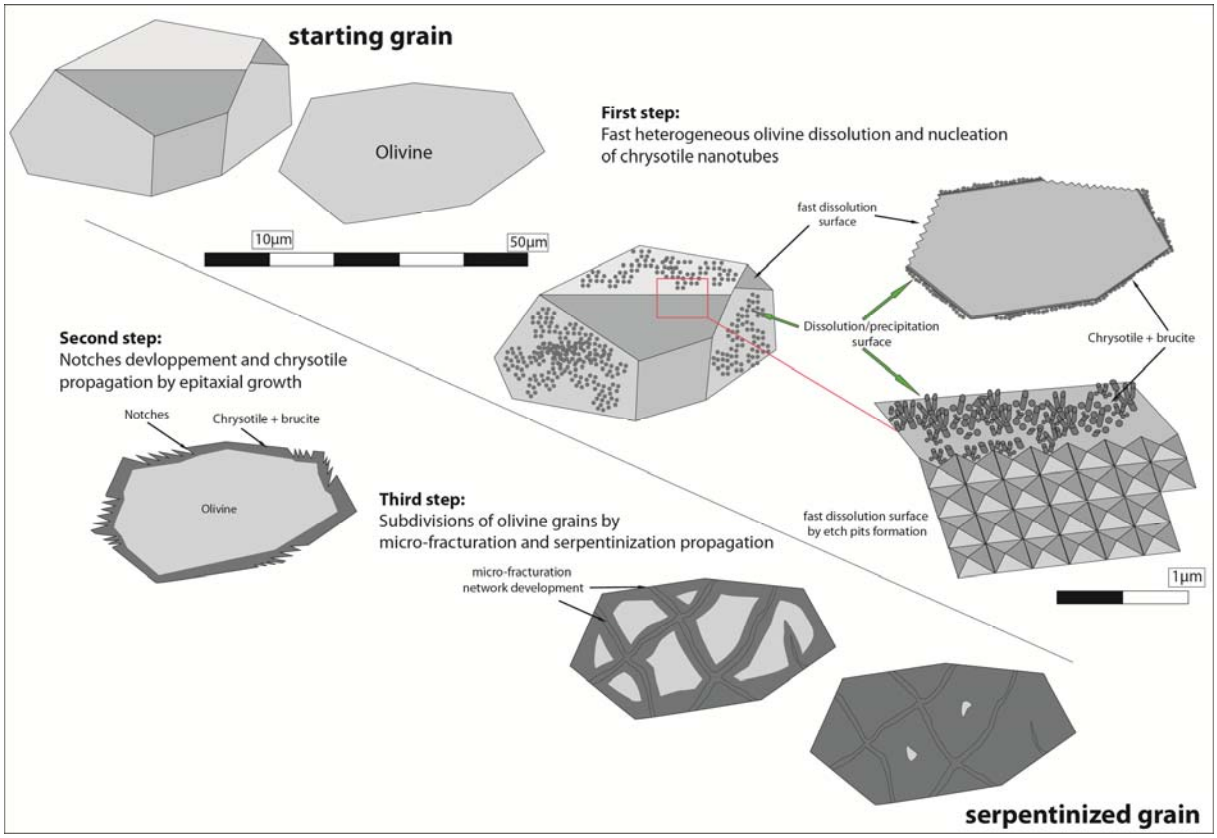

583